

Systematic local simulations of fast neutrino flavor conversions with scattering effects

Milad Delfan Azari

*Waseda Research Institute for Science and Engineering,
Waseda University, 3-4-1 Okubo, Shinjuku, Tokyo 169-8555, Japan and
Department of Physics, Graduate School of Advanced Science and Engineering,
Waseda University, 3-4-1 Okubo, Shinjuku, Tokyo 169-8555, Japan*

Hirokazu Sasaki

Los Alamos National Laboratory, Los Alamos, New Mexico 87545, USA

Tomoya Takiwaki

National Astronomical Observatory of Japan, 2-21-1 Osawa, Mitaka, Tokyo 181-8588, Japan

Hirotsada Okawa

Waseda Institute for Advanced Study, Waseda University, Tokyo 169-0051, Japan

(Dated: February 8, 2024)

We investigate the dynamics of fast neutrino flavor conversions (FFCs) in the one-dimensional (1D) inhomogeneous and the homogeneous models as post processes by employing snapshots obtained by our self-consistent, realistic Boltzmann simulations in two spatial dimensions (2D). We show that the FFC growth rate is considerably larger in the inhomogeneous model than in the homogeneous model, as expected from the previous linear analysis results. We find that the momentum space dimension does not significantly influence the neutrino transition probability under inhomogeneous conditions. On the other hand, in the homogeneous model without collisions, the FFC depends on the momentum space, and the azimuthal angle dependence breaks the periodicity of the FFC. Our study demonstrates that collision-induced enhancement occurs on a long time scale in the inhomogeneous model. Despite that collision-induced enhancement does not appear on the short time scale, that should be taken into account to predict the final conversion probability.

I. INTRODUCTION

Neutrinos are the most abundant massive particles in the universe [1]. Although they are massive, their masses are much smaller than those of their charged lepton counterparts. Due to the mismatch between their flavor and mass eigenstates, they can experience flavor transformation when propagating through vacuum [2, 3]. Weak interactions with surrounding matter can change the dispersion relation in vacuum and induce resonant conversions known as the MSW (Mikheyev-Smirnov-Wolfenstein) effect [4]. In a dense neutrino environment, due to the high population of neutrinos, interaction with other neutrinos generates their own self-energy, which can lead to collective neutrino oscillations [5–10].

Massive stars ($M_\star \gtrsim 8 M_\odot$) at the end of their lives may explode as core-collapse supernovae (CCSNe). During this event, about 10^{53} erg energy is released in an enormous amount of neutrinos in all flavors (ν_e , ν_μ and ν_τ). It is believed that these neutrinos are essential ingredients in CCSNe's explosion mechanism. If a fraction of ν_e and $\bar{\nu}_e$ are reabsorbed by the matter between the shock front and the so-called gain radius and deposit their energy to push the stagnated shock again, CCSNe are expected. It is known that ν_μ , ν_τ and their anti-particles have higher energies than ν_e and $\bar{\nu}_e$ due to the weak interactions of ν_μ , $\bar{\nu}_\mu$, ν_τ and $\bar{\nu}_\tau$ with matters while propagating. If the former neutrinos (ν_μ , $\bar{\nu}_\mu$, ν_τ and $\bar{\nu}_\tau$)

are converted to the latter neutrinos (ν_e and $\bar{\nu}_e$), those converted neutrinos will be absorbed by matter. Such neutrino flavor conversion transfers more neutrino energy to the matter behind the shock, resulting in either a successful explosion or a failure of the shock revive [11–14]. Therefore, collective neutrino oscillations have attracted the most attention since about a decade ago. However, their mechanisms are still unknown due to their non-linearity and complex nature.

In particular, among collective neutrino oscillations, the fast flavor conversion (FFC) has been speculated to occur deep inside CCSNe. The frequency is proportional to the neutrino potential $\mu \sim \sqrt{2}G_F n_\nu$ [15–17] and high enough to ignore the vacuum frequency. The linear stability analysis was used to reveal the growth of the FFC before solving the non-linear evolution. It has been pointed out that FFC occurs as a result of the crossing between the angular distribution of electron-type neutrinos ν_e and anti-electron neutrinos $\bar{\nu}_e$, the so-called electron-lepton number (ELN) crossing [18, 19]. The possibility of FFC in CCSNe has been studied intensively as post processes using neutrino radiation hydrodynamic simulations [20–25]. Even though the fact that angular crossings in neutrino-flavor-lepton-numbers (NFLN), which are necessary and sufficient conditions for FFC, are unlikely to occur in spherically symmetric CCSN models, they have been observed more frequently in multidimensional models [26, 27].

Many simulations have recently been performed to

understand the non-linear evolution beyond the linear regime, solving the time evolution of FFC. Most of them treat small-scale local areas [e.g., 28–35]. Several large-scale global simulations are performed with the parameter rescaling technique [36–38]. The effect of collisions has also been investigated in terms of their effect on FFC [39, 40]. Some papers reported that neutral-current collisions enhance fast flavor conversions (e.g., [41–43]), while others have reported damping effects [44–46]. Although these previous studies focused on the energy-integrated neutrino angular distribution, energy-dependent scattering, emission, and absorption are also studied [47–49]. Ref. [43] pointed out the inconsistency of the initial profile and the setting of the numerical simulation. A similar but different mechanism, collisional instability, is also found and discussed so far [48, 50, 51]. Some of the results seem controversial with each other, and the overall role of collisions in fast flavor conversion is still unclear.

The goal of this paper is to investigate FFCs in a non-linear regime and the effect of neutrino-nucleon scatterings by examining the dynamics of four flavors of neutrinos ($\nu_e, \bar{\nu}_e, \nu_x$, and $\bar{\nu}_x$) in both homogeneous and one-dimensional inhomogeneous setups. The dimension of momentum spaces is systematically changed, and the initial condition is taken from the realistic two-dimensional (2D) fully self-consistent Boltzmann-neutrino-radiation-hydrodynamics simulations. This article is organized as follows. In Section II, we introduce the equations that are used in our analysis. Section III presents detailed information on our models. In Section IV, we show our results, and finally, in Section V, we summarize our results and conclude the paper.

II. FORMULATION

Similar to the previous works [42, 52–55], we calculate fast neutrino flavor conversions of ν_e and ν_x with their anti-particles $\bar{\nu}_e$ and $\bar{\nu}_x$ considering the collision effects of neutrino scattering. We use QDSCNO code [Sasaki and Takiwaki (2022), hereafter we call this S22, 42] to study the neutrino flavor conversions based on the neutrino density matrices. The evolution of neutrinos is described as

$$\partial_t \rho + v_i \partial_i \rho = -i [H, \rho] + C(\rho, \bar{\rho}), \quad (1)$$

$$\partial_t \bar{\rho} + v_i \partial_i \bar{\rho} = -i [\bar{H}, \bar{\rho}] + \bar{C}(\rho, \bar{\rho}), \quad (2)$$

where ρ , H and C are density matrix, Hamiltonian, and collision terms for neutrinos, respectively. $\bar{\rho}$, \bar{H} and \bar{C} correspond to those for anti-neutrinos. v_i is the velocity of the neutrino for i -direction. In this study, we consider one spatial dimension z and $v_z = c \cos \theta_\nu$, where c is the speed of light.

In this study, for simplicity, we use two flavor approximation. The density matrix consists of independent components, $\rho_{ij}, \bar{\rho}_{ij}$, where $i, j = e, x$. Note that those are Hermitian matrix, i.e., $\rho_{ij} = \rho_{ji}^*$, where $*$ is complex conjugate. The initial density matrix is normalized by the

neutrino distribution function, and can be written as

$$\rho_{ii}(E_\nu, \theta_\nu, \phi_\nu) = 4\pi f_{\nu_i}(E_\nu, \theta_\nu, \phi_\nu) / n_{E, \nu_e}, \quad (3)$$

$$n_{E, \nu_e}(E_\nu) = \int d\Omega_\nu f_{\nu_e}, \quad (4)$$

where $d\Omega_\nu = \sin \theta_\nu d\theta_\nu d\phi_\nu$. E_ν is the energy, and θ_ν and ϕ_ν are angles in the momentum space and f_{ν_i} denotes the distribution function of ν_i . Here we consider a three-dimensional momentum space. In some models, we reduce the number of dimensions and the definition for one- or two-dimensional momentum space is shown in Appendix A.

The left hand sides in Eqs. (1) and (2) are solved by 5th-order WENO method. For the time-integration, Runge-Kutta 4th method is used. This part is not taken into account in the previous version of QDSCNO [42]. For the details of WENO, see COSE ν [56] and GRQKNT [57]. A code comparison is performed in Ref. [58]. We also test the problem in Ref. [58], which is presented in Appendix B.

The Hamiltonian in Eqs. (1) and (2) is written as

$$H = H_{\text{vacuum}} + H_{\text{matter}} + H_{\nu\nu}, \quad (5)$$

where the vacuum term is given as

$$H_{\text{vacuum}} = \frac{\Delta m^2}{4E_\nu} \begin{pmatrix} -\cos \theta_\nu & \sin \theta_\nu \\ \sin \theta_\nu & \cos \theta_\nu \end{pmatrix}, \quad (6)$$

where $\Delta m^2 = 2.5 \times 10^{-6} \text{ eV}^2$. Note that we impose an effective vacuum mixing angle $\theta_\nu = 10^{-6}$ instead of the matter potential.

The collective part is given as

$$H_{\nu\nu}(\theta_\nu, \phi_\nu) = \int d\mu'_E \int \frac{d\phi'_\nu}{2\pi} \int_{-1}^1 \frac{d \cos \theta'_\nu}{2} h_{\nu\nu}, \quad (7)$$

where $d\mu'_E$ is

$$d\mu'_E = \sqrt{2} G_F \frac{E_\nu'^2 dE'_\nu}{(2\pi\hbar c)^3} n_{E, \nu_e}, \quad (8)$$

and $h_{\nu\nu}$ is

$$\begin{aligned} h_{\nu\nu} = & [\rho(E'_\nu, \theta'_\nu, \phi'_\nu) - \bar{\rho}(E'_\nu, \theta'_\nu, \phi'_\nu)] \\ & \times [1 - \cos \theta_\nu \cos \theta'_\nu - \sin \theta_\nu \sin \theta'_\nu \\ & \times (\cos \phi_\nu \cos \phi'_\nu + \sin \phi_\nu \sin \phi'_\nu)]. \end{aligned} \quad (9)$$

The collision terms in Eqs. (1) and (2) are similar to the Eq. (2) and (8) in Ref. [59] (see also Refs. [42, 44]). Considering the collision terms of neutrino scattering in Neutral-Current (NC) reactions and employing the elastic neutrino-nucleon collisions, we have

$$C^{\text{NC}}(\rho) = -\kappa_0 \rho + \int \frac{d\Omega'_\nu}{4\pi} \left(\kappa_0 - \frac{\kappa_1}{3} \cos \theta_\nu \cos \theta'_\nu \right) \rho', \quad (10)$$

$$\bar{C}^{\text{NC}}(\bar{\rho}) = -\kappa_0 \bar{\rho} + \int \frac{d\Omega'_\nu}{4\pi} \left(\kappa_0 - \frac{\kappa_1}{3} \cos \theta_\nu \cos \theta'_\nu \right) \bar{\rho}', \quad (11)$$

where $\rho' = \rho(E_\nu, \theta'_\nu, \phi'_\nu)$ and $\bar{\rho}' = \bar{\rho}(E_\nu, \theta'_\nu, \phi'_\nu)$. Here, the non-axisymmetric scattering is ignored. The coefficients in the NC collision terms are given by [44]

$$\kappa_0 = \frac{3G^2 E_\nu^2}{\pi} \sum_{N=n,p} n_N \left\{ (c_A^N)^2 + \frac{(c_V^N)^2}{3} \right\}, \quad (12)$$

$$\kappa_1 = \frac{3G^2 E_\nu^2}{\pi} \sum_{N=n,p} n_N \{ (c_A^N)^2 - (c_V^N)^2 \}, \quad (13)$$

where $n_N (= n_n, n_p)$ is the nucleon number density inside the matter.

We also consider the effect of Charged-Current (CC) reactions by employing the collision term of neutrino-electron scatterings [59],

$$C^{\text{CC}}(\rho) = -\Gamma^{\text{CC}} \begin{pmatrix} \rho_{ee} & \frac{\rho_{ex}}{2} \\ \frac{\rho_{xe}}{2} & 0 \end{pmatrix} + \Gamma^{\text{CC}} \begin{pmatrix} \int \frac{d\Omega'_\nu}{4\pi} \rho'_{ee} & 0 \\ 0 & 0 \end{pmatrix}, \quad (14)$$

$$\bar{C}^{\text{CC}}(\bar{\rho}) = -\bar{\Gamma}^{\text{CC}} \begin{pmatrix} \bar{\rho}_{ee} & \frac{\bar{\rho}_{ex}}{2} \\ \frac{\bar{\rho}_{xe}}{2} & 0 \end{pmatrix} + \bar{\Gamma}^{\text{CC}} \begin{pmatrix} \int \frac{d\Omega'_\nu}{4\pi} \bar{\rho}'_{ee} & 0 \\ 0 & 0 \end{pmatrix}, \quad (15)$$

where the $\Gamma^{\text{CC}} = 1/\lambda_{\nu_e e}$, $\bar{\Gamma}^{\text{CC}} = 1/\lambda_{\bar{\nu}_e e}$ and mean free path λ are calculated from the net electron density n_e and the neutrino scattering cross section $\sigma_{\nu_\alpha e}$ [59],

$$\Gamma^{\text{CC}} = \frac{1}{\lambda_{\nu_e e}} \sim n_e (\sigma_{\nu_e e} - \sigma_{\nu_x e}), \quad (16)$$

$$\bar{\Gamma}^{\text{CC}} = \frac{1}{\lambda_{\bar{\nu}_e e}} \sim n_e (\sigma_{\bar{\nu}_e e} - \sigma_{\bar{\nu}_x e}), \quad (17)$$

where

$$\sigma_i = \frac{3}{8} \sigma_0 c_i \left(k_B T + \frac{\mu_e}{4} \right) \frac{E_\nu}{(m_e c^2)^2}. \quad (18)$$

$c_i = 2.333, 1.0, 0.3$ and $0, 3$ for $\nu_e, \bar{\nu}_e, \nu_\mu, \bar{\nu}_\mu$, respectively [60]. That depends on the temperature, T and the chemical potential of electron μ_e . Here $\sigma_0 = 1.7 \times 10^{-44} \text{ cm}^2$. On this collision, the elastic approximation is not applicable [e.g., 61], but we assume it for simplicity. Ref. [62] is helpful for finding more detailed equations that include emission and absorption.

III. MODELS

In this section, we provide detailed information on our models. The initial conditions in this article are provided by Delfan Azari et al. (2019) [20] and Delfan Azari et al. (2020) [21], hereafter we call these references D19 and D20. The first paper (D19) did not find any ELN crossing but the second paper (D20) obtained the ELN crossing in the protoneutron star (PNS) region. These results are favorable to our study and are the main motivation to conduct this research.

The initial profile is taken from the results of the realistic two-dimensional (2D) fully self-consistent Boltzmann-neutrino-radiation-hydrodynamics simulations for the progenitor model of non-rotating $11.2 M_\odot$ [63] which were performed on the Japanese K-supercomputer [64]. In these simulations, three neutrino species, $\nu_e, \bar{\nu}_e$, and ν_x are considered, and their distributions are computed on spherical coordinates (r, θ) under spatial axisymmetry. We employed spherical coordinates in momentum space $(E_\nu, \theta_\nu, \phi_\nu)$, in which the two angles are measured from the local radial direction. The computational domain covers $0 \leq r \leq 5000 \text{ km}$, $0 \leq \theta \leq \pi$, $0 \leq E_\nu \leq 300 \text{ MeV}$, $0 \leq \theta_\nu \leq \pi$ and $0 \leq \phi_\nu \leq 2\pi$ with 384 (r), 128 (θ), 20 (E_ν), 10 (θ_ν) and 6 (ϕ_ν) mesh cells. The paper adopts the Furusawa-Shen equation of state (FSEOS) that is based on relativistic mean field theory for nuclear matter [65].

In this article, we present only the results of our analysis at the post-bounce time of $t_{\text{pb}} = 190 \text{ ms}$. We chose this time because, we found the crossing for the first time at a point at the radius $r = 16.5 \text{ km}$ and the spatial zenith $\theta = 2.1 \text{ rad}$ at the post-bounce time of $t_{\text{pb}} = 190 \text{ ms}$ in D20 [21].

The hydrodynamic properties of this point is summarized as follows. The density, ρ_B , is $2.4 \times 10^{13} \text{ g/cm}^3$; electron fraction, Y_e , is 0.13; temperature, $k_B T$, is 20.4 MeV; and the chemical potential of electron, μ_e , is 56.9 MeV. The values are summarized in Table I.

TABLE I. Summary of variables and values.

Variable	Symbol	Value
baryon density	ρ_B	$2.4 \times 10^{13} \text{ g/cm}^3$
electron fraction	Y_e	0.13
temperature	T	20.4 MeV
chemical potential of electrons	μ_e	56.9 MeV
averated neutrino energy	$\langle E_\nu \rangle$	64.0 MeV
potential of neutrino	μ	$1.93 \times 10^{13} \text{ s}^{-1}$
peak of dispersion relation	Ω_{peak}	$3.9 \times 10^{10} \text{ s}^{-1}$
typical growth rate of P_{tra} in inhomogeneous model	Ω_{IH}	$\sim 8 \times 10^{10} \text{ s}^{-1}$
typical growth rate of P_{tra} in homogeneous model	Ω_{HO}	$\sim 8 \times 10^8 \text{ s}^{-1}$
typical growth rate of P_{tra} in the late period in S1M1-LCC	$\Omega_{\text{S1M1-LCC}}$	$\sim 1.5 \times 10^6 \text{ s}^{-1}$
NC-collision rate	κ_0	$0.43 \times 10^8 \text{ s}^{-1}$
NC-collision rate	κ_1	$0.17 \times 10^8 \text{ s}^{-1}$
CC-collision rate for ν_e	Γ^{CC}	$0.058 \times 10^8 \text{ s}^{-1}$
CC-collision rate for $\bar{\nu}_e$	$\bar{\Gamma}^{\text{CC}}$	$0.018 \times 10^8 \text{ s}^{-1}$
growth rate of collisional instability	Ω_{CI}	$0.406 \times 10^6 \text{ s}^{-1}$

Using the initial profile, we systematically investigate the effects of dimension and collision. Table II summarizes our models. We perform simulations of homogeneous and one-dimensional inhomogeneous simulations. The model names are written in the form of S and M. We call inhomogeneous model S1 since its spatial dimension is one and homogenous model S0 whose spatial dimension is zero. The direction of z is taken as r direction in the background model. For the momentum space, we have

TABLE II. In this table, we summarize the properties of models. The model names are written in the form of S and M, in which M stands for the dimension of momentum space, and S corresponds to the dimension of space, i.e., S1 and S0 denote inhomogeneous and homogeneous models, respectively. The meaning of the model name is also written in the description column. The numerical resolution of the simulation is summarized in $N_{\theta_\nu}, N_{\phi_\nu}, N_{E_\nu}, N_z$ columns as well. Results column summarizes the feature of transition probability. S0M1 and S1M1 are the fiducial models in the homogenous and inhomogeneous models, respectively. We show the feature of models comparing their evolution of the probability to that of the fiducial model. Finally, previous works using similar setup are summarized in References column.

Homogeneous models							
Model	Description	N_{θ_ν}	N_{ϕ_ν}	N_{E_ν}	N_z	Results	References
S0M1	S0: Homogeneous	200	1	1	1	Periodic, fiducial	[e.g., 41, 42]
S0M1-NC	NC: Neutral-Current scattering	200	1	1	1	Suppressed	[41]
S0M1-CC	CC: Charged-Current scattering	200	1	1	1	Enhanced	[42, 50]
S0M2E	M2E: Energy-dependent	100	1	30	1	not affected	[47]
S0M2E-NC		100	1	30	1	Enhanced	[47]
S0M2E-CC		100	1	30	1	Enhanced	
S0M2A	M2A: Azimuth-dependent	100	100	1	1	Break periodicity	[35]
S0M2A-NC		100	100	1	1	Suppressed	
S0M2A-CC		100	100	1	1	Enhanced	
S0M3	M3: 3D momentum space	100	100	30	1	Break periodicity	
S0M3-NC		100	100	30	1	Enhanced	
S0M3-CC		100	100	30	1	Enhanced	
Inhomogeneous models							
Model	Description	N_{θ_ν}	N_{ϕ_ν}	N_{E_ν}	N_z	Results	References
S1M1	S1: Inhomogeneous	200	1	1	1024	fiducial	[e.g., 44, 45]
S1M1-HP	HP: Homogeneous perturbations	200	1	1	1024	Suppressed	
S1M1-NC		200	1	1	1024	not affected	[44, 45]
S1M1-CC		200	1	1	1024	not affected	
S1M1-L	L: long-term	200	1	1	1024	fiducial	
S1M1-LNC		200	1	1	1024	Slightly enhanced	
S1M1-LCC		200	1	1	1024	Enhanced	[50]
S1M2E		100	1	30	1024	not affected	
S1M2E-NC		100	1	30	1024	not affected	
S1M2E-CC		100	1	30	1024	not affected	
S1M2A		100	100	1	1024	not affected	
S1M2A-NC		100	100	1	1024	not affected	
S1M2A-CC		100	100	1	1024	not affected	
S1M3		40	40	10	1024	not affected	
S1M3-NC		40	40	10	1024	not affected	
S1M3-CC		40	40	10	1024	not affected	

four choices, M1, M2E, M2A and M3 where their degree of freedom is (θ_ν) , (E_ν, θ_ν) , (θ_ν, ϕ_ν) , and $(E_\nu, \theta_\nu, \phi_\nu)$, respectively. In each model, remaining dimension is integrated (see Appendix A). In the model name, M stands for the dimension of momentum space.

We also change the type of the scattering. In the model name, NC and CC are used for Neutral-Current and Charged-Current, see Eqs. (10)–(15), for the description.

The initial noise level is controlled as follows.

$$\rho_{ex} = (\rho_{ee} + \rho_{xx})(\epsilon_r + \epsilon_i \imath), \quad (19)$$

$$\bar{\rho}_{ex} = (\bar{\rho}_{ee} + \bar{\rho}_{xx})(\bar{\epsilon}_r + \bar{\epsilon}_i \imath), \quad (20)$$

where $\epsilon_r, \epsilon_i, \bar{\epsilon}_r, \bar{\epsilon}_i$ are the random number that is less than 10^{-8} . Note that ρ_{ex} and $\bar{\rho}_{ex}$ are complex numbers and ϵ_r, ϵ_i are real numbers. We impose this perturbation in all degrees of freedom. For example, in S1M1 model, different values of $\epsilon_r, \epsilon_i, \bar{\epsilon}_r, \bar{\epsilon}_i$ are used for each z and θ_ν grid.

IV. RESULTS

We start showing our results by illustrating the initial condition of M1 (energy integrated axisymmetric) profile in Figure 1. The density matrix of $\nu_e, \bar{\nu}_e, \nu_x$ is shown as red, blue, and green, respectively. Note that $\bar{\nu}_x = \nu_x$. The position of electron-lepton number (ELN) crossing is indicated by the text and it occurs at $\cos \theta_\nu \sim 0.3$.

A. Dependence on dimension

We describe the dynamics of neutrino oscillation by beginning with fiducial model, S1M1. We then discuss the effects of spatial dimension and momentum space dimension.

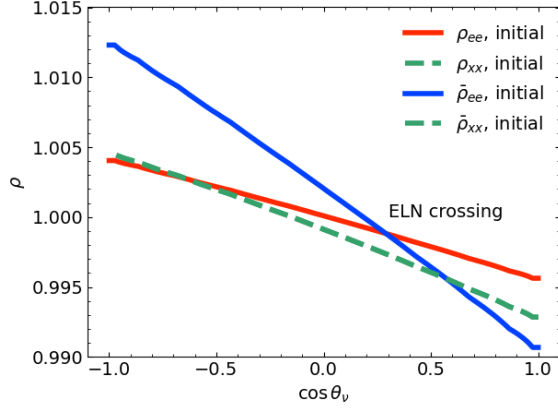


FIG. 1. Initial condition of M1 (energy integrated axisymmetric) simulation. ρ_{ee} (red), $\bar{\rho}_{ee}$ (blue), ρ_{xx} and $\bar{\rho}_{xx}$ (green) correspond to the density matrix of ν_e , $\bar{\nu}_e$, ν_x and $\bar{\nu}_x$, respectively. Initially $\rho_{xx} = \bar{\rho}_{xx}$. The position of electron-lepton number crossing is indicated by the text. See Appendix A to obtain M1 density matrix. Note that our notation assumes $\int \frac{d \cos \theta_\nu}{2} \rho_{ee} = 1$ and that would be factor 2 larger than some works that assume $\int d \cos \theta_\nu \rho_{ee} = 1$.

1. fiducial model

Let us see the fiducial model, S1M1, which is performed in one spatial dimension, z , and one momentum dimension θ_ν . This setup is called an inhomogeneous setup. The range of spatial coordinates, z , covers $-10 \text{ cm} \leq z \leq 10 \text{ cm}$. As written in Table II, the grid number for z is $N_z = 1024$ and the grid number for θ_ν is $N_{\theta_\nu} = 200$. As in S22 [42], we use Gauss-Legendre grid to minimize the error in the integration of θ_ν . The self-interaction Hamiltonian, Eq. (A6), is characterized by $\mu = 1.93 \times 10^{13} \text{ s}^{-1}$. The average energy is calculated by Eq. (A7) and is used in Eq. (6), see Table I.

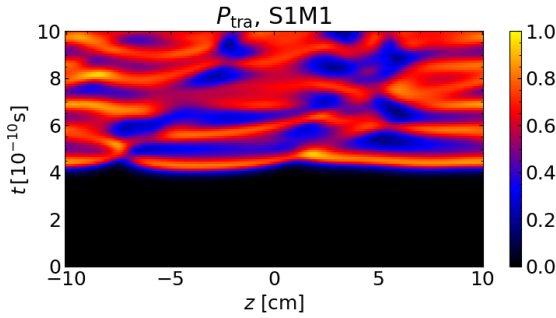


FIG. 2. Transition probability of S1M1 model is written in space-time diagram.

Overall evolution of S1M1 is depicted in Figure 2, which shows spatial and time evolution of transition

probability,

$$P_{\text{tra}} = \frac{\langle \rho_{ee} \rangle_{\text{ini}} - \langle \rho_{ee} \rangle}{\langle \rho_{ee} \rangle_{\text{ini}} - \langle \rho_{xx} \rangle_{\text{ini}}}, \quad (21)$$

where $\langle A \rangle$ is a average of the quantity, A . In Figure 2, $P_{\text{tra}}(z; t)$ is shown and $\langle A \rangle = \int d \cos \theta_\nu A / 2$.

At $t = 4 \times 10^{-10} \text{ s}$, we observe a significant increase of the transition probability. Thus, the growth rate is $\Omega_{\text{IH}} \sim 8 \times 10^{10} \text{ s}^{-1}$. Since we impose random perturbation in all area, the instability grows everywhere. In Fig. 4 of D20 [21], the linear growth rate is a few 10^{10} s^{-1} . Our result is consistent with this estimate. After the first peak, the conversion probability oscillates with the timescale of 10^{-10} s . This oscillation is also seen in the previous works [e.g., 33, 58]. The neutrino propagates with the speed of light, i.e., 3 cm per 10^{-10} s . The pattern of P_{tra} also propagates with the speed of light.

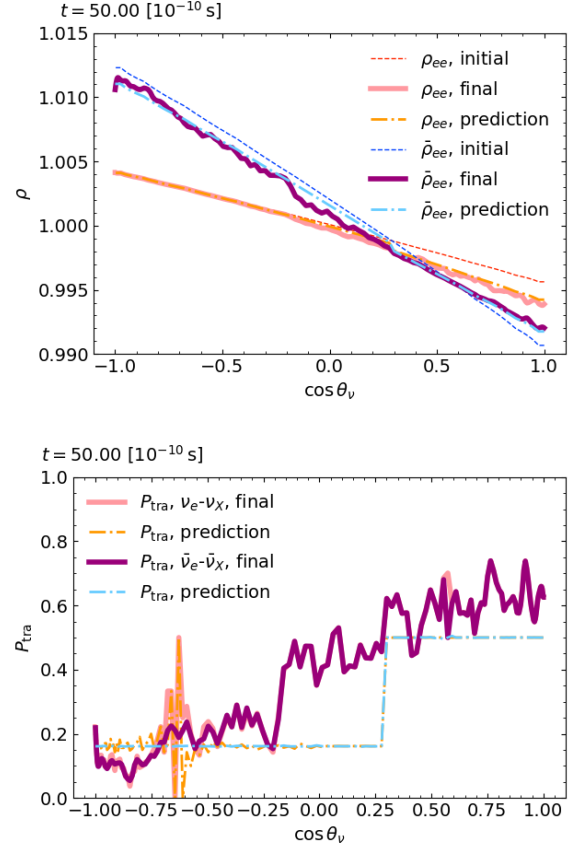


FIG. 3. Top: The initial and final states of the density matrix of S1M1 model are shown as a function of $\cos \theta_\nu$. ρ_{ee} (dashed red) and $\bar{\rho}_{ee}$ (dashed blue) correspond to the density matrix of initial ν_e and $\bar{\nu}_e$, respectively (same as Figure 1). The final states of ρ_{ee} and $\bar{\rho}_{ee}$ are indicated by pink and purple solid lines, respectively. The theoretical prediction is given by orange and dashed-dotted sky blue line for ν_e and $\bar{\nu}_e$, respectively. Bottom: The transition probability is shown. The color of the line is the same as that of the top panel.

After $t = 10 \times 10^{-10} \text{ s}$, the oscillation state reaches

equilibrium. Top panel of Figure 3 shows the initial and final profile of the density matrix, the snapshot of $t = 50 \times 10^{-10}$ s. In the region of $0.3 \leq \cos \theta_\nu \leq 1$, ρ_{ee} decreases and $\bar{\rho}_{ee}$ increases and the initial difference of density matrix is mitigated. A series of works is devoted to predict the asymptotic state of the neutrino [28, 66–70]. In our cases, we can use the formula for periodic boundary, i.e., Eqs. (22) and (23) of Ref. [68]. We plot the theoretical prediction in orange (ν_e) and sky blue (ν_x) curves in Figure 3. Our final state roughly agrees with the prediction. In the region of $0.3 \leq \cos \theta_\nu \leq 1$, the survival probability is ~ 0.5 and the survival probability of other region is determined by the lepton number conservation. In the bottom panel, we explicitly show the transition probability using the spatial average, $\langle A \rangle = \frac{1}{z_{\max} - z_{\min}} \int dz A$ in Eq.(21). The fluctuation pattern changes by time. We may obtain a smoother profile using time averaging. The regions of $0.3 \leq \cos \theta_\nu$ and $\cos \theta_\nu \leq -0.25$ agree with the prediction. Note that at $\cos \theta_\nu \sim -0.7$, the denominator in Eq. (21), $\langle \rho_{ee} \rangle_{\text{ini}} - \langle \rho_{xx} \rangle_{\text{ini}}$, becomes zero (see Figure 1) and we cannot define the transition probability and numerical round-off error appears in the panel. In the middle region, the theoretical prediction discontinuously jumps from left to right at $\cos \theta_\nu = 0.3$, but the simulation result is smooth, connecting the two regions. We may need a more detailed formula for a more precise prediction [e.g., 70].

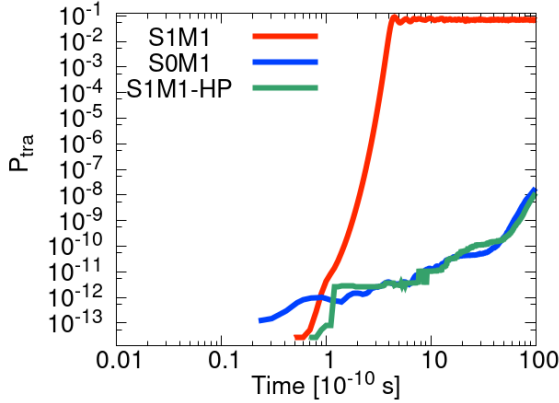


FIG. 4. Comparison of S0M1, S1M1, and S1M1-HP in the time evolution of transition probability.

2. spatial dimension

To see the effect of spatial dimension, we compare the inhomogeneous model with the homogeneous model. Here homogenous means the advection term in Eqs. (1) and (2) is ignored.

The transition probability depends on the spatial dimension and the shape of the perturbations. Figure 4 shows the time evolution of the transition probability of

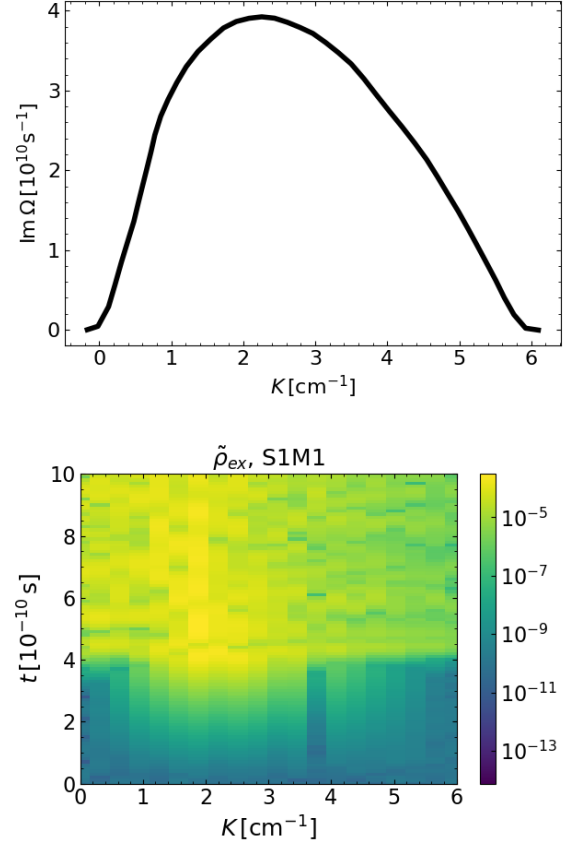


FIG. 5. Top: The dispersion relation of FFC, which is similar to the one we obtained in D20 [21]. The peak of the growth rate, Ω_{peak} is $3.9 \times 10^{10} \text{ s}^{-1}$, see Table I. Bottom: The evolution of the Fourier component of $\text{Re}(\rho_{ex})$ in the S1M1 model.

S0M1, S1M1, and S1M1-HP. In S1M1 and S1M1-HP, we evaluate the spatial average of the probability where the spatial and angle average are taken in $\langle A \rangle$ in Eq. (21).

The growth of the instability in the homogeneous model (blue) is significantly slower, $\Omega_{\text{HO}} \sim 8 \times 10^8 \text{ s}^{-1}$, than that of inhomogeneous model (red) in Figure 4, which is summarized in Table I. This is because the growth rate of the instability depends on the wave number and the homogeneous model does not capture the most rapidly growing mode. The linear growth rate of this initial condition is evaluated in D20 [21]. In the linear analysis, we usually take

$$\rho = \frac{\rho_{ee,\text{ini}} + \rho_{xx,\text{ini}}}{2} + \frac{\rho_{ee,\text{ini}} - \rho_{xx,\text{ini}}}{2} \begin{pmatrix} s & S \\ S^* & -s \end{pmatrix}, \quad (22)$$

where $|s|^2 + |S|^2 = 1$. The evolution of the non-diagonal component of density matrix, S , is proportional to $e^{-i(\Omega t - \mathbf{K} \cdot \mathbf{x})}$, which is associated with the wave number vector \mathbf{K} . Taking K as the wave number of the radially outward direction, we show the dispersion relation in the top panel of Figure 5. From the magenta curve in Fig. 4 of D20 [21], we need to shift the wave number following

$-k = K - \Phi$, and $\Phi = \int \frac{d\cos\theta_\nu}{2} G_\nu \cos\theta_\nu$, where k is the wave number of the radially inward direction of neutrinos and G_ν is the ELN angular distribution including neutrino distributions (see D20 [21] for more details). From the initial neutrino distributions, we can calculate G_ν and obtain $\Phi \sim 1.5 \text{ cm}^{-1}$.

In the homogeneous setup, only the $K = 0$ mode can be captured. In the top panel of Figure 5, the growth rate at $K = 0$ is significantly lower than the most rapidly growing mode at $K \sim 2 \text{ cm}^{-1}$. This is the reason why the homogeneous model shows a very slow growth compared to the inhomogeneous model.

On the other hand, the inhomogeneous setup allows the finite value of K and the mode with $1 \text{ cm}^{-1} < K < 5 \text{ cm}^{-1}$ can grow relatively rapidly. This is confirmed in the bottom panel of Figure 5, which shows the Fourier component of $\text{Re}(\rho_{ex})$ as a function of time and wave number in the S1M1 model. In the linear growth phase ($t < 4 \times 10^{-10} \text{ s}$), the mode with $1 \text{ cm}^{-1} < K < 5 \text{ cm}^{-1}$ grows (yellow). In the non-linear phase ($t > 4 \times 10^{-10} \text{ s}$), the Fourier component extends more widely. Such a widely spread spectrum is also found in Ref. [58], see their Fig. 3. On the growth rate, the most rapidly growing mode is Ω_{peak} is $3.9 \times 10^{10} \text{ s}^{-1}$ in Figure 5 and is consistent with one in the simulation, $\Omega_{\text{IH}} \sim 8 \times 10^{10} \text{ s}^{-1}$. Note that transition probability in linear phase is written as $P_{\text{tra}} \sim \frac{1}{4}|S|^2 \propto \exp(2\Omega_{\text{peak}}t) \sim \exp(\Omega_{\text{IH}}t)$.

The previous interpretation is confirmed in more detailed analysis. S1M1-HP in Fig. 4 shows the result of the same inhomogeneous model as S1M1 while using the different spatial perturbation at $t = 0 \text{ s}$ i.e.,

$$\rho_{ex}(\theta_\nu, z) = \rho_{ex}(\theta_\nu, 0), \quad (23)$$

$$\bar{\rho}_{ex}(\theta_\nu, z) = \bar{\rho}_{ex}(\theta_\nu, 0), \quad (24)$$

which mimics the homogeneous model. The same perturbation is used for all positions. The growth of the transition probability in S1M1-HP (green) is similar to that of S0M1 (blue) after $t = 10^{-10} \text{ s}$ and significantly slower than that of S1M1 (red) due to the homogeneous perturbation in Eqs. (23) and (24). In Table II, we summarize the results of the transition probability and write "Suppressed" in the line of S1M1-HP.

3. momentum space dimension

In the inhomogeneous setup, the dimension of momentum space does not significantly change the transition probability. Figure 6 shows the time evolution of the transition probability of S1M1, S1M2E, S1M2A, and S1M3. The definition of the transition probability is similar to Eq. (21) but the averaging depends on the dimension. In Table II, we summarize the results of transition probability and note "not affected" in the line of these models.

One spatial and one momentum (1+1) dimensions may be enough to capture the feature of the instability for

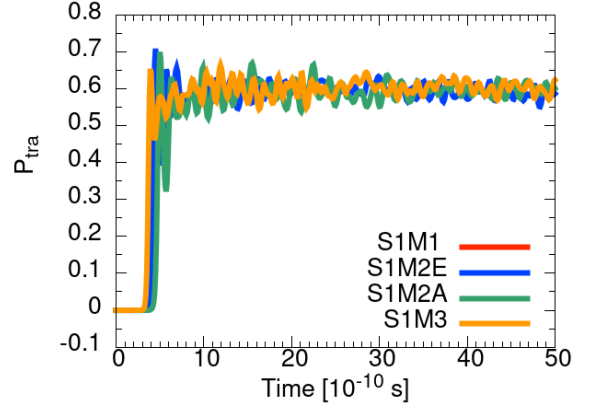


FIG. 6. Dependence of the momentum space dimension in the time evolution of the transition probability. In the top panel, we compare S1M1 (red), S1M2E (blue), S1M2A (green), and S1M3 (orange) to see the dependence of the momentum space dimension in the inhomogeneous models.

our initial profile. Top panel of Figure 7 shows $\rho_{ee} - \bar{\rho}_{ee}$ of S1M2A at the initial phase. That is almost axisymmetric. The red region ($\rho_{ee} - \bar{\rho}_{ee} > 0$) and blue region ($\rho_{ee} - \bar{\rho}_{ee} < 0$) is divided by $\cos\theta_\nu \sim 0.3$, which is similar to that of angle averaged profile (see Figure 1). In the bottom panel of Figure 7, the final transition probability is shown. The profile is almost axisymmetric and is not so different from the angle averaged profile (see Figure 3). Ref. [34] also shows that the spatial dimension does not change the transition probability in their fiducial axisymmetric setup. If the initial profile deviates from axisymmetry, the results would depend on the spatial and momentum space dimensions. Looking to the top panel of Figure 7 more carefully, we found slight azimuthal dependent structures, $\rho_{ee} - \bar{\rho}_{ee} = 0$ near $(\cos\theta_\nu, \phi_\nu) = (0, \pi)$, and that does not disappear in the bottom panel.

From the result of S1M2E, we conclude that the averaged properties are more critical to determine the final phase than the detailed energy-dependent properties. Our initial condition of S1M2E depends on the neutrino energy and the left panel of Figure 8 shows the initial ELN crossing profiles. In the right panel, the spectrum $\frac{\partial n_{\nu_e}}{\partial E_\nu}$, is shown. The definition is $\frac{\partial n_{\nu_e}}{\partial E_\nu} = \iint \frac{E_\nu^2 d\Omega_\nu}{(2\pi\hbar c)^3} f_{\nu_e}$. The peak of spectrum is $\sim 50 \text{ MeV}$ and ELN crossing appears in $\cos\theta_\nu \sim 0.3$, which is consistent with the energy-integrated profile in Figure 1. The position of ELN crossing in the low-energy region ($E_\nu < 20 \text{ MeV}$) is almost $\cos\theta_\nu \sim 0$ and there is no ELN crossing in the high-energy region ($E_\nu > 100 \text{ MeV}$). These are different from the averaged profile, where ELN crossing appears in $\cos\theta_\nu \sim 0.3$ (see Figure 1). These deviations from the averaged profile do not significantly change the final transition probability. Figure 9 shows the transition probability as a function of $\cos\theta_\nu$ and E_ν . The probability does not depend on the energy and that in $0.3 < \cos\theta_\nu < 1$ becomes equilibrium, ~ 0.5 . This feature is similar to

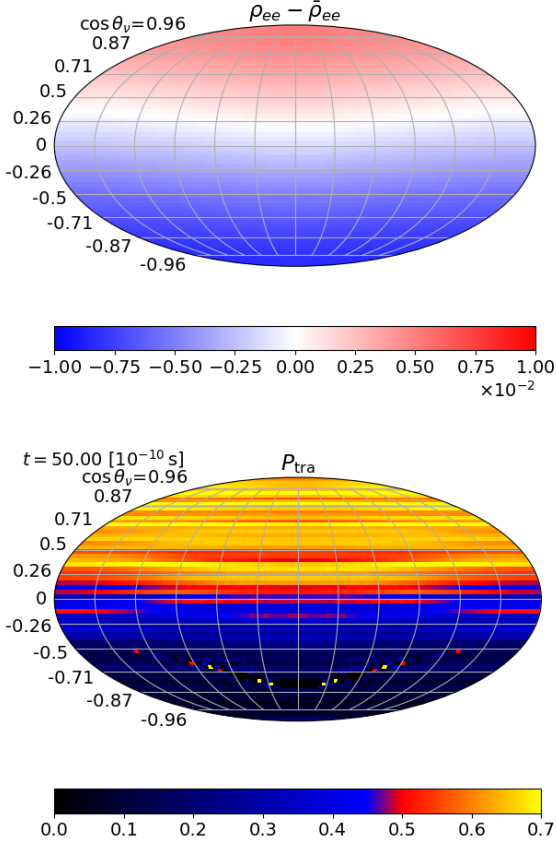


FIG. 7. Top: The initial profile of S1M2A. Initial $\rho_{ee} - \bar{\rho}_{ee}$ is displayed in Mollweide projection. Bottom: The transition probability of the final profile in S1M2A. In both panels, the north pole corresponds to $\theta_\nu = 0$, and the vertical ticks are written in $\cos \theta_\nu$. The west and east ends correspond to $\phi_\nu = 0$ or 2π .

that of energy-integrated profile (see Figure 3).

In the homogeneous setup, the non-axisymmetric motion significantly alters the transition probability. Figure 10 shows the time evolution of the transition probabilities of S0M1, S0M2E, S0M2A, and S0M3. The periodic motion of S0M1 is associated with the axisymmetric feature (only θ'_ν dependence) in Eq. (A6) and is consistent with the previous homogeneous calculations [41, 42, 47]. S0M2E shows periodic motion similar to S0M1 because the fast oscillation mode without collision is induced by the dependence of the neutrino angular distribution and the E'_ν dependence in Eq. (A13) has minor effects on the fast mode although such energy dependence is the origin of the slow mode [5]. On the other hand, S0M2A breaks the periodicity and significantly alters the flavor conversion. Such a broken periodicity is induced by non-axisymmetric term ϕ'_ν in Eq. (A19) and is consistent with the result in Ref. [35]. The evolution of S0M3 is same as S0M2A. In Table II, we note "Break periodicity" in S0M2A and S0M3. In the absence of collision, the fast flavor conversions in

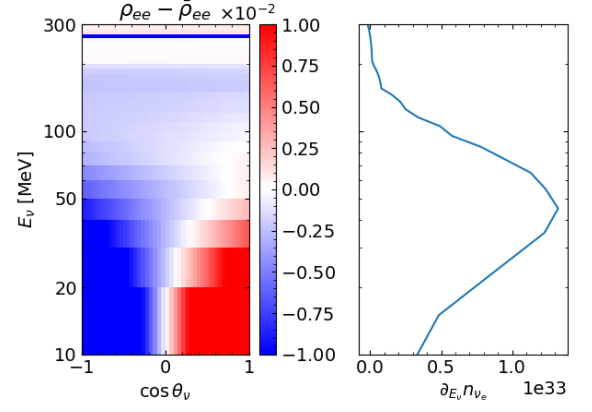


FIG. 8. The initial profile of M2E simulations. Left: The initial $\rho_{ee} - \bar{\rho}_{ee}$ is displayed as a function of E_ν and $\cos \theta_\nu$. Here, the color bar scales as 10^{-2} . Right: The number spectrum of electron type neutrino, $\frac{\partial n_{\nu_e}}{\partial E_\nu}$. The vertical axis is the same as the left panel, E_ν .

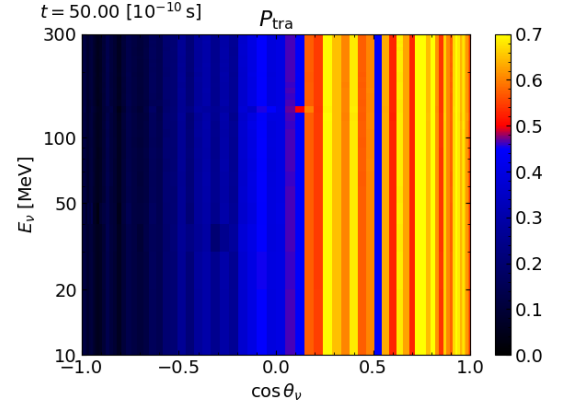


FIG. 9. The final transition probability of S1M2E. The probability is written as a function of $\cos \theta_\nu$ and E_ν .

the homogeneous model are significantly affected by the ϕ_ν dependence although such non-axisymmetric effect is smeared out in the inhomogeneous model. Such feature is also confirmed in the flavor conversions involving collision terms as shown in the next section.

B. Effect of collision

Collision does not strongly change the transition probability in the inhomogeneous setup. Figure 11 shows the time evolution of the transition probability of 12 inhomogeneous models. The four types of momentum dimensions (M1, M2A, M2E, M3) and three collisions (none, -NC, -CC) are considered. We do not observe any significant enhancement or suppression compared to S1M1.

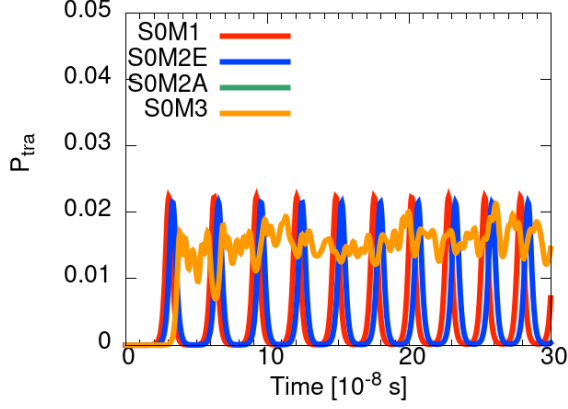


FIG. 10. Dependence of the momentum space dimension in time evolution of transition probability. We compare S0M1 (red), S0M2E (blue), S0M2A (green), and S0M3 (orange) to see the dependence in the homogeneous models. S0M2A (green) overlaps S0M3 (orange) and is not visible in the figure.

It is consistent with Ref. [44, 45]. They also claim that the collision does not affect the transition probability. In this study, this fact is confirmed more systematically. In Table II, we note that "not affected" in the line of these models.

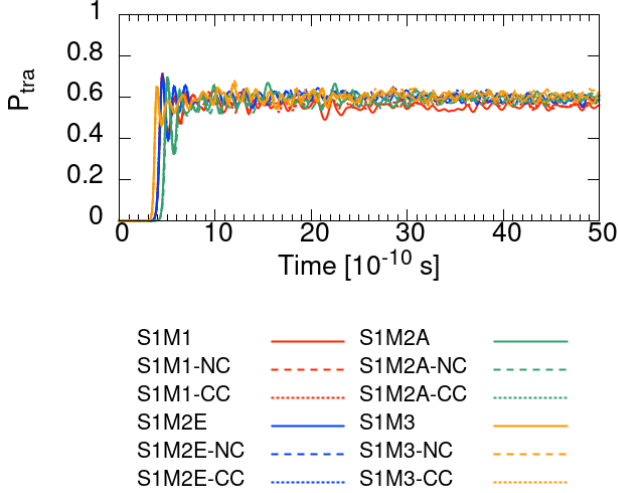


FIG. 11. Effect of the scattering in the inhomogeneous setup. The evolution of transition probability of 12 models are compared. The models with four types of momentum space dimensions are displayed, i.e., S1M1, S1M2E, S1M2A and S1M3. In these models, we add two types of collision, -NC and -CC.

An interesting feature is found in a long-term simulation. Figure 12 compares the transition probability of S1M1-L, S1M1-LNC, and S1M1-LCC. The simulation time is extended to $t = 30 \times 10^{-8}$ s (the fiducial model, S1M1, is carried out until $t = 1 \times 10^8$ s). We found a slight

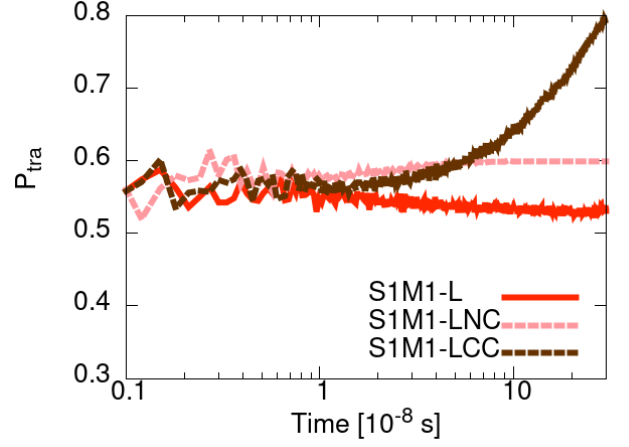


FIG. 12. A long-term evolution of transition probability in the inhomogeneous setup with scattering. S1M1-L, S1M1-LNC, and S1M1-LCC are colored in red, pink, and brown, respectively.

increase in transition probability in S1M1-LNC (pink line). Here $\kappa_0 \sim 0.43 \times 10^8 \text{ s}^{-1}$ and $\kappa_1 \sim 0.17 \times 10^8 \text{ s}^{-1}$ in Eq. (12), compare other rates in Table I. Compare it to the other instability in Table I. The effect of the collision appears after $t \geq 10^{-8}$ s. At the final epoch ($t \sim 30 \times 10^{-8}$ s), the angular distributions of neutrinos in S1M1-LNC become completely flat. Remember that this initial condition is taken from the radius of 19 km, which is inside the neutrino sphere. The isotropic angular distribution can be achieved in this environment. Note that the neutrino is moving ~ 0.09 km during 30×10^{-8} s and the matter density and collision rate become smaller (larger) during outward (inward) propagation. To make the setup realistic, we may need to employ the Dirichlet boundary condition [36, 37, 57, 69] instead of the periodic boundary condition, which we currently use.

We found a significant improvement in probability in S1M1-LCC. We speculate on the enhancement as a collisional instability [50] that is triggered by the difference between the collision rate of ν_e and $\bar{\nu}_e$. The instability criterion is shown in Eq.(6) in Ref. [50] and is written as

$$\frac{n_{\bar{\nu}_e} - n_{\bar{\nu}_x}}{n_{\nu_e} - n_{\nu_x}} \geq \frac{\bar{\Gamma}^{\text{CC}}}{\Gamma^{\text{CC}}}. \quad (25)$$

The emission and absorption can contribute to this instability but those are ignored in this study (see Ref. [48] for the model with those). The neutrino density is written as $n_i = n_\nu + \delta n_i$ where $n_\nu = 1.0 \times 10^{35} \text{ cm}^{-3}$. At $t = 1 \times 10^{-8}$ s, $(\delta n_{\nu_e}, \delta n_{\bar{\nu}_e}, \delta n_{\nu_x}, \delta n_{\bar{\nu}_x}) = (1.84, 2.65, 2.0, 3.1) \times 10^{32} \text{ cm}^{-3}$. Those are initially $(2.44, 4.31, 1.44, 1.44) \times 10^{32} \text{ cm}^{-3}$. $\Gamma^{\text{CC}} = 0.058 \times 10^8 \text{ s}^{-1}$ and $\bar{\Gamma}^{\text{CC}} = 0.018 \times 10^8 \text{ s}^{-1}$, which is significantly lower than the growth rate of FFC, Ω_{IH} , see Table I. Substituting these values, we found that our system is unstable.

We evaluate the growth rate of the instability in our model at $t = 5 \times 10^{-8}$ s in Figure 12, and the rate is

$\Omega_{\text{S1M1-LCC}} = 1.5 \times 10^6 \text{ s}^{-1}$. As expected, the growth rate is slower than FFC (see Table I). Theoretically, we can also evaluate the growth rate, Ω_{CI} , using Eq. (14) in Ref. [50] (see also Ref. [49, 51]) and

$$\Omega_{\text{CI}} \sim \frac{\Gamma^{\text{CC}} - \bar{\Gamma}^{\text{CC}}}{2} \frac{n_{\nu_e} - n_{\nu_x} + n_{\bar{\nu}_e} - n_{\bar{\nu}_x}}{|n_{\nu_e} - n_{\nu_x} - n_{\bar{\nu}_e} + n_{\bar{\nu}_x}|} - \frac{\Gamma^{\text{CC}} + \bar{\Gamma}^{\text{CC}}}{2}. \quad (26)$$

Substituting the values at $t = 1 \times 10^{-8} \text{ s}$, we obtain $\Omega_{\text{CI}} \sim 0.406 \times 10^6 \text{ s}^{-1}$. This value is closer to that is observed in our simulation.

In contrast to FFC in the inhomogeneous setup (see Figure 11), the collision strongly changes the transition probability in the homogeneous configuration. Figures 13 and 14 show the time evolution of the transition probability of models with NC collision and CC collision, respectively. Models without collision are also shown by thin solid lines. The same colors as in Figure 10 are used for momentum dimension, i.e., S0M1 (red), S0M2E (blue), S0M2A (green), S0M3 (orange).

It is difficult to quantify the effects of NC collision. The transition probability is shown in Figures 13. While S0M1-NC and S0M2A-NC show the suppression of the transition probability compared to those without the collision term, S0M2E-NC and S0M3-NC show the enhancement of the probability. The flavor conversion of S0M1-NC is more suppressed than that of S0M1. Such suppression from NC collisions was also confirmed in Ref. [42] when κ_0^{-1} and κ_1^{-1} are comparable to the timescale of FFC, see Table I. Similar to our energy dependent simulations, S0M2E-NC and S0M3-NC, Refs. [47, 71] also report the enhancement of conversion probability. Ref. [47] reports that we need to change the average energy in the collision term to keep the consistency between the energy-dependent and the energy-averaged simulations. In this study, we calculate $\langle E_\nu \rangle$ following Eq. (A7) and use it in the collision term.

CC-collision basically enhances the transition probability. We summarize our results in Figures 14. While S0M1-CC and S0M2E-CC show a slight enhancement, S0M2A-CC and S0M3-CC show a significant increase. This means that the azimuthal-angle dependence is important in CC-collisions. As discussed in the long-term simulations of inhomogeneous setup (see Figure 12), collisional instability also occurs with FFC. The timescale of the collisional instability is slower than that of FFC but it increases the growth rate in the late epoch.

V. SUMMARY AND DISCUSSION

We calculate FFCs with collision effects of neutrino scatterings based on the realistic initial profile that is taken from two-dimensional (2D) fully self-consistent Boltzmann-neutrino-radiation-hydrodynamics simulations for the progenitor model of non-rotating $11.2 M_\odot$ which were performed on the Japanese K-supercomputers at the post-bounce time of $t_{\text{pb}} = 190$

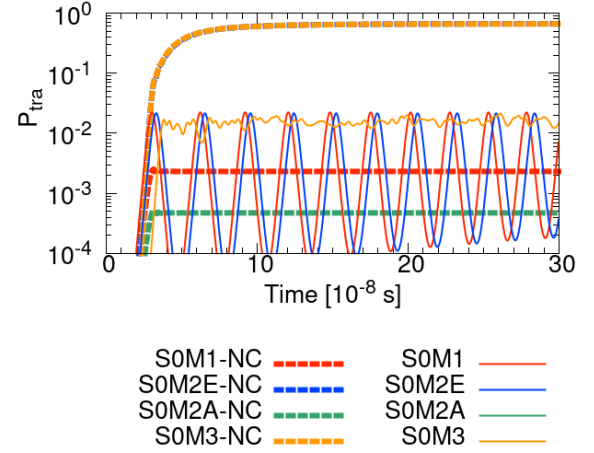


FIG. 13. The effect of NC-collision in homogeneous models. The logarithmic transition probability is shown as a function of time. Dashed lines are used for the NC-collision models, whereas thin solid lines are used for the models without collision. Similar to Figure 10, momentum dimension is indicated by color, i.e., S0M1 (red), S0M2E (blue), S0M2A (green), S0M3 (orange). S0M2A (solid green) overlaps S0M3 (solid orange) and is not visible in the figure. Similarly, S0M2E-NC (dashed blue) overlaps S0M3-NC (dashed orange) and is not visible in the figure.

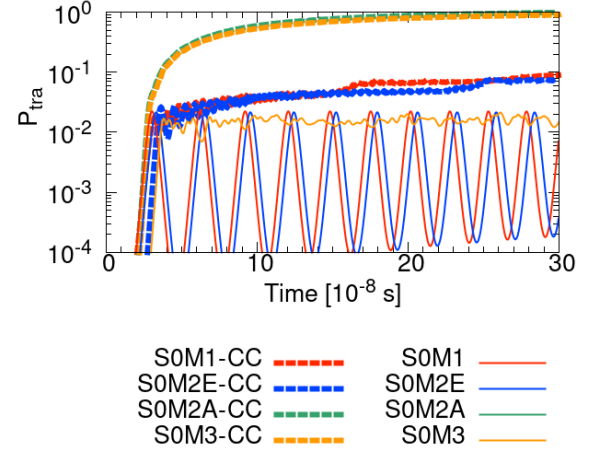


FIG. 14. The effect of CC-collision in homogeneous models. Same to Figure 13, but the impact of CC-collision is displayed. S0M2A (solid green) overlaps S0M3 (solid orange) and is not visible in the figure. Similarly, S0M2A-CC (dashed green) overlaps S0M3-CC (dashed orange) and is not visible in the figure.

ms.

The effect of spatial dimension is examined by comparing the 1D inhomogeneous model with the homogeneous model. The transition probability depends on the spatial dimension and the shape of the perturbations. The growth of instability in the homogeneous model is significantly slower than that of the inhomogeneous model because the growth rate on the wave number K , and the

homogeneous model does not capture the most rapidly growing mode.

The dimension of momentum space does not significantly affect the transition probability in the inhomogeneous model. We demonstrate that the averaged properties are more critical for determining the final phase than the detailed energy-dependent properties. In our initial condition, all flavors have similar number density and spectrum. Even if a significant transition probability is observed, this hardly affects the explodability and observation. A non-axisymmetric motion significantly alters the transition probability in the homogeneous model. In the absence of collision, the fast flavor conversions in the homogeneous model are strongly affected by the azimuthal angle dependence. However, such a non-axisymmetric effect is smeared out in the inhomogeneous model.

The collision-induced enhancement occurs on a long time scale in the inhomogeneous model. Such enhancement does not appear on the short-time scale in the inhomogeneous model despite its prominence in the homogeneous model. We hypothesize that the enhancement is caused by collisional instability caused by the difference between ν_e and $\bar{\nu}_e$ collision rates [50].

Our current analysis depends on the mean-field approximation, however, the many-body effect should be considered [see 10, 72, 73, and references therein]. For the inhomogeneous model, the periodic boundary condition is employed, but the Dirichlet boundary can be considered [28, 66–70]. The results depend on the boundary condition, and such a simplified setup could be different from the realistic setup in supernovae [43]. We may

need further discussion on this issue. So far, we consider neutrino scattering. Emission and absorption [48] and other processes [70] should be considered in the future. Even though we used a two-flavor approximation in this paper, extending the formulation to three flavors is certainly necessary [74, 75]. We remark that our FFC calculation is decoupled from the 2D CCSN simulation and the feedback from FFC to hydrodynamics [11–13] is not taken into account. Further development will be needed for self-consistent implementation [e.g., 14, 70].

ACKNOWLEDGMENTS

We thank Shoichi Yamada, Hiroki Nagakura, Chinami Kato, Masamichi Zaizen, Sherwood Richers, and Lucas Johns for fruitful discussions and useful comments. This study was supported in part by JSPS/MEXT KAKENHI Grant Numbers JP21H01083, JP21H01088, JP22H01223, JP23H01199 and JP23K03400. Numerical computations were carried out on GPU and PC cluster at the Center for Computational Astrophysics, National Astronomical Observatory of Japan. This research was also supported by MEXT as “Program for Promoting researches on the Supercomputer Fugaku” (Structure and Evolution of the Universe Unraveled by Fusion of Simulation and AI; Grant Number JPMXP1020230406) and JICFuS. This work was carried out under the auspices of the National Nuclear Security Administration of the U.S. Department of Energy at Los Alamos National Laboratory under Contract No. 89233218CNA000001.

-
- [1] V. A. Kostelecký and S. Samuel, Neutrino oscillations in the early universe with nonequilibrium neutrino distributions, *Phys. Rev. D* **52**, 3184 (1995).
 - [2] Y. Fukuda et al. (Super-Kamiokande), Evidence for oscillation of atmospheric neutrinos, *Phys. Rev. Lett.* **81**, 1562 (1998), [arXiv:hep-ex/9807003](#).
 - [3] J. Gava and C. Volpe, Collective neutrino oscillations in matter and CP violation, *Phys. Rev. D* **78**, 083007 (2008).
 - [4] L. Wolfenstein, Neutrino oscillations in matter, *Phys. Rev. D* **17**, 2369 (1978).
 - [5] H. Duan, G. M. Fuller, and Y.-Z. Qian, Collective neutrino oscillations, *Annual Review of Nuclear and Particle Science* **60**, 569 (2010), <https://doi.org/10.1146/annurev.nucl.012809.104524>.
 - [6] A. Mirizzi, I. Tamborra, H. T. Janka, N. Saviano, K. Scholberg, R. Bollig, L. Hudepohl, and S. Chakraborty, Supernova neutrinos: production, oscillations and detection, *Nuovo Cimento Rivista Serie* **39**, 1 (2016), [arXiv:1508.00785 \[astro-ph.HE\]](#).
 - [7] I. Tamborra and S. Shalgar, New Developments in Flavor Evolution of a Dense Neutrino Gas, *arXiv e-prints*, [arXiv:2011.01948](#) (2020), [arXiv:2011.01948 \[astro-ph.HE\]](#).
 - [8] F. Capozzi and N. Saviano, Neutrino Flavor Conversions in High-Density Astrophysical and Cosmological Environments, *Universe* **8**, 94 (2022), [arXiv:2202.02494 \[hep-ph\]](#).
 - [9] S. Richers and M. Sen, Fast Flavor Transformations, *arXiv e-prints*, [arXiv:2207.03561](#) (2022), [arXiv:2207.03561 \[astro-ph.HE\]](#).
 - [10] M. C. Volpe, Neutrinos from dense: flavor mechanisms, theoretical approaches, observations, new directions, *arXiv e-prints*, [arXiv:2301.11814](#) (2023), [arXiv:2301.11814 \[hep-ph\]](#).
 - [11] Y. Suwa, K. Kotake, T. Takiwaki, M. Liebendörfer, and K. Sato, Impacts of collective neutrino oscillations on core-collapse supernova explosions, *The Astrophysical Journal* **738**, 165 (2011).
 - [12] J. Ehring, S. Abbar, H.-T. Janka, G. Raffelt, and I. Tamborra, Fast neutrino flavor conversion in core-collapse supernovae: A parametric study in 1D models, *Phys. Rev. D* **107**, 103034 (2023), [arXiv:2301.11938 \[astro-ph.HE\]](#).
 - [13] J. Ehring, S. Abbar, H.-T. Janka, G. Raffelt, and I. Tamborra, Fast Neutrino Flavor Conversions Can Help and Hinder Neutrino-Driven Explosions, *Phys. Rev. Lett.* **131**, 061401 (2023), [arXiv:2305.11207 \[astro-ph.HE\]](#).
 - [14] H. Nagakura, Roles of Fast Neutrino-Flavor Conver-

- sion on the Neutrino-Heating Mechanism of Core-Collapse Supernova, *Phys. Rev. Lett.* **130**, 211401 (2023), [arXiv:2301.10785 \[astro-ph.HE\]](#).
- [15] R. F. Sawyer, Multiangle instability in dense neutrino systems, *Phys. Rev. D* **79**, 105003 (2009).
 - [16] R. F. Sawyer, Neutrino cloud instabilities just above the neutrino sphere of a supernova, *Phys. Rev. Lett.* **116**, 081101 (2016).
 - [17] R. F. Sawyer, Speed-up of neutrino transformations in a supernova environment, *Phys. Rev. D* **72**, 045003 (2005).
 - [18] L. Johns and H. Nagakura, Fast flavor instabilities and the search for neutrino angular crossings, *Phys. Rev. D* **103**, 123012 (2021), [arXiv:2104.04106 \[hep-ph\]](#).
 - [19] B. Dasgupta, Collective Neutrino Flavor Instability Requires a Crossing, *Phys. Rev. Lett.* **128**, 081102 (2022), [arXiv:2110.00192 \[hep-ph\]](#).
 - [20] M. Delfan Azari, S. Yamada, T. Morinaga, W. Iwakami, H. Okawa, H. Nagakura, and K. Sumiyoshi, Linear analysis of fast-pairwise collective neutrino oscillations in core-collapse supernovae based on the results of boltzmann simulations, *Phys. Rev. D* **99**, 103011 (2019).
 - [21] M. Delfan Azari, S. Yamada, T. Morinaga, H. Nagakura, S. Furusawa, A. Harada, H. Okawa, W. Iwakami, and K. Sumiyoshi, Fast collective neutrino oscillations inside the neutrino sphere in core-collapse supernovae, *Phys. Rev. D* **101**, 023018 (2020).
 - [22] S. Abbar, H. Duan, K. Sumiyoshi, T. Takiwaki, and M. C. Volpe, On the occurrence of fast neutrino flavor conversions in multidimensional supernova models, *Phys. Rev. D* **100**, 043004 (2019), [arXiv:1812.06883 \[astro-ph.HE\]](#).
 - [23] S. Abbar, H. Duan, K. Sumiyoshi, T. Takiwaki, and M. C. Volpe, Fast neutrino flavor conversion modes in multidimensional core-collapse supernova models: The role of the asymmetric neutrino distributions, *Phys. Rev. D* **101**, 043016 (2020), [arXiv:1911.01983 \[astro-ph.HE\]](#).
 - [24] S. Abbar, Searching for fast neutrino flavor conversion modes in core-collapse supernova simulations, *J. Cosmology Astropart. Phys.* **2020**, 027 (2020), [arXiv:2003.00969 \[astro-ph.HE\]](#).
 - [25] S. Abbar, F. Capozzi, R. Glas, H. T. Janka, and I. Tamborra, On the characteristics of fast neutrino flavor instabilities in three-dimensional core-collapse supernova models, *Phys. Rev. D* **103**, 063033 (2021), [arXiv:2012.06594 \[astro-ph.HE\]](#).
 - [26] S. Shalgar and I. Tamborra, On the Occurrence of Crossings between the Angular Distributions of Electron Neutrinos and Antineutrinos in the Supernova Core, *ApJ* **883**, 80 (2019), [arXiv:1904.07236 \[astro-ph.HE\]](#).
 - [27] H. Nagakura, A. Burrows, L. Johns, and G. M. Fuller, Where, when, and why: Occurrence of fast-pairwise collective neutrino oscillation in three-dimensional core-collapse supernova models, *Phys. Rev. D* **104**, 083025 (2021), [arXiv:2108.07281 \[astro-ph.HE\]](#).
 - [28] B. Dasgupta, A. Mirizzi, and M. Sen, Simple method of diagnosing fast flavor conversions of supernova neutrinos, *Phys. Rev. D* **98**, 103001 (2018), [arXiv:1807.03322 \[hep-ph\]](#).
 - [29] F. Capozzi, M. Chakraborty, S. Chakraborty, and M. Sen, Mu-Tau Neutrinos: Influencing Fast Flavor Conversions in Supernovae, *Phys. Rev. Lett.* **125**, 251801 (2020), [arXiv:2005.14204 \[hep-ph\]](#).
 - [30] L. Johns, H. Nagakura, G. M. Fuller, and A. Burrows, Neutrino oscillations in supernovae: Angular moments and fast instabilities, *Phys. Rev. D* **101**, 043009 (2020), [arXiv:1910.05682 \[hep-ph\]](#).
 - [31] C. Kato, H. Nagakura, Y. Hori, and S. Yamada, Neutrino Transport with Monte Carlo Method. I. Toward Fully Consistent Implementation of Nucleon Recoils in Core-collapse Supernova Simulations, *ApJ* **897**, 43 (2020), [arXiv:2001.11148 \[astro-ph.HE\]](#).
 - [32] C. Kato, H. Nagakura, and T. Morinaga, Neutrino Transport with the Monte Carlo Method. II. Quantum Kinetic Equations, *ApJS* **257**, 55 (2021), [arXiv:2108.06356 \[astro-ph.HE\]](#).
 - [33] M.-R. Wu, M. George, C.-Y. Lin, and Z. Xiong, Collective fast neutrino flavor conversions in a 1D box: Initial conditions and long-term evolution, *Phys. Rev. D* **104**, 103003 (2021), [arXiv:2108.09886 \[hep-ph\]](#).
 - [34] S. Richers, D. Willcox, and N. Ford, Neutrino fast flavor instability in three dimensions, *Phys. Rev. D* **104**, 103023 (2021), [arXiv:2109.08631 \[astro-ph.HE\]](#).
 - [35] S. Shalgar and I. Tamborra, Symmetry breaking induced by pairwise conversion of neutrinos in compact sources, *Phys. Rev. D* **105**, 043018 (2022), [arXiv:2106.15622 \[hep-ph\]](#).
 - [36] H. Nagakura and M. Zaizen, Time-Dependent and Quasisteady Features of Fast Neutrino-Flavor Conversion, *Phys. Rev. Lett.* **129**, 261101 (2022), [arXiv:2206.04097 \[astro-ph.HE\]](#).
 - [37] H. Nagakura and M. Zaizen, Connecting small-scale to large-scale structures of fast neutrino-flavor conversion, *Phys. Rev. D* **107**, 063033 (2023), [arXiv:2211.01398 \[astro-ph.HE\]](#).
 - [38] Z. Xiong, M.-R. Wu, G. Martínez-Pinedo, T. Fischer, M. George, C.-Y. Lin, and L. Johns, Evolution of collisional neutrino flavor instabilities in spherically symmetric supernova models, *Phys. Rev. D* **107**, 083016 (2023), [arXiv:2210.08254 \[astro-ph.HE\]](#).
 - [39] V. Cirigliano, M. W. Paris, and S. Shalgar, Effect of collisions on neutrino flavor inhomogeneity in a dense neutrino gas, *Physics Letters B* **774**, 258 (2017), [arXiv:1706.07052 \[hep-ph\]](#).
 - [40] F. Capozzi, B. Dasgupta, A. Mirizzi, M. Sen, and G. Sigl, Collisional Triggering of Fast Flavor Conversions of Supernova Neutrinos, *Phys. Rev. Lett.* **122**, 091101 (2019), [arXiv:1808.06618 \[hep-ph\]](#).
 - [41] S. Shalgar and I. Tamborra, Change of direction in pairwise neutrino conversion physics: The effect of collisions, *Phys. Rev. D* **103**, 063002 (2021), [arXiv:2011.00004 \[astro-ph.HE\]](#).
 - [42] H. Sasaki and T. Takiwaki, A detailed analysis of the dynamics of fast neutrino flavor conversions with scattering effects, *Progress of Theoretical and Experimental Physics* **2022**, 073E01 (2022), [arXiv:2109.14011 \[hep-ph\]](#).
 - [43] L. Johns and H. Nagakura, Self-consistency in models of neutrino scattering and fast flavor conversion, *Phys. Rev. D* **106**, 043031 (2022), [arXiv:2206.09225 \[hep-ph\]](#).
 - [44] J. D. Martin, J. Carlson, V. Cirigliano, and H. Duan, Fast flavor oscillations in dense neutrino media with collisions, *Phys. Rev. D* **103**, 063001 (2021).
 - [45] G. Sigl, Simulations of fast neutrino flavor conversions with interactions in inhomogeneous media, *Phys. Rev. D* **105**, 043005 (2022).
 - [46] I. Padilla-Gay, I. Tamborra, and G. G. Raffelt, Neutrino fast flavor pendulum. II. Collisional damping,

- Phys. Rev. D **106**, 103031 (2022), arXiv:2209.11235 [hep-ph].
- [47] C. Kato and H. Nagakura, Effects of energy-dependent scatterings on fast neutrino flavor conversions, Phys. Rev. D **106**, 123013 (2022), arXiv:2207.09496 [astro-ph.HE].
- [48] C. Kato, H. Nagakura, and M. Zaizen, Flavor conversions with energy-dependent neutrino emission and absorption, Phys. Rev. D **108**, 023006 (2023), arXiv:2303.16453 [astro-ph.HE].
- [49] Y.-C. Lin and H. Duan, Collision-induced flavor instability in dense neutrino gases with energy-dependent scattering, Phys. Rev. D **107**, 083034 (2023), arXiv:2210.09218 [hep-ph].
- [50] L. Johns, Collisional Flavor Instabilities of Supernova Neutrinos, Phys. Rev. Lett. **130**, 191001 (2023).
- [51] J. Liu, M. Zaizen, and S. Yamada, Systematic study of the resonancelike structure in the collisional flavor instability of neutrinos, Phys. Rev. D **107**, 123011 (2023), arXiv:2302.06263 [hep-ph].
- [52] S. Yamada, Boltzmann equations for neutrinos with flavor mixings, Phys. Rev. D **62**, 093026 (2000).
- [53] A. Vlasenko, G. M. Fuller, and V. Cirigliano, Neutrino quantum kinetics, Phys. Rev. D **89**, 105004 (2014).
- [54] S. Shalgar and I. Tamborra, Change of direction in pairwise neutrino conversion physics: The effect of collisions, Phys. Rev. D **103**, 063002 (2021).
- [55] D. N. Blaschke and V. Cirigliano, Neutrino quantum kinetic equations: The collision term, Phys. Rev. D **94**, 033009 (2016).
- [56] M. George, C.-Y. Lin, M.-R. Wu, T. G. Liu, and Z. Xiong, COSE ν : A collective oscillation simulation engine for neutrinos, Computer Physics Communications **283**, 108588 (2023), arXiv:2203.12866 [hep-ph].
- [57] H. Nagakura, General-relativistic quantum-kinetics neutrino transport, Phys. Rev. D **106**, 063011 (2022), arXiv:2206.04098 [astro-ph.HE].
- [58] S. Richers, H. Duan, M.-R. Wu, S. Bhattacharyya, M. Zaizen, M. George, C.-Y. Lin, and Z. Xiong, Code comparison for fast flavor instability simulations, Phys. Rev. D **106**, 043011 (2022), arXiv:2205.06282 [astro-ph.HE].
- [59] L. Johns, Collisional Flavor Instabilities of Supernova Neutrinos, Phys. Rev. Lett. **130**, 191001 (2023), arXiv:2104.11369 [hep-ph].
- [60] R. L. Bowers and J. R. Wilson, A numerical model for stellar core collapse calculations., ApJS **50**, 115 (1982).
- [61] M. Rampp and H. T. Janka, Radiation hydrodynamics with neutrinos. Variable Eddington factor method for core-collapse supernova simulations, A&A **396**, 361 (2002), arXiv:astro-ph/0203101 [astro-ph].
- [62] S. A. Richers, G. C. McLaughlin, J. P. Kneller, and A. Vlasenko, Neutrino Quantum Kinetics in Compact Objects, Phys. Rev. D **99**, 123014 (2019), arXiv:1903.00022 [astro-ph.HE].
- [63] S. E. Woosley, A. Heger, and T. A. Weaver, The evolution and explosion of massive stars, Rev. Mod. Phys. **74**, 1015 (2002).
- [64] H. Nagakura, W. Iwakami, S. Furusawa, H. Okawa, A. Harada, K. Sumiyoshi, S. Yamada, H. Matsufuru, and A. Imakura, Simulations of core-collapse supernovae in spatial axisymmetry with full boltzmann neutrino transport, The Astrophysical Journal **854**, 136 (2018).
- [65] S. Furusawa, K. Sumiyoshi, S. Yamada, and H. Suzuki, New equations of state based on the liquid drop model of heavy nuclei and quantum approach to light nuclei for core-collapse supernova simulations, The Astrophysical Journal **772**, 95 (2013).
- [66] S. Bhattacharyya and B. Dasgupta, Late-time behavior of fast neutrino oscillations, Phys. Rev. D **102**, 063018 (2020).
- [67] S. Bhattacharyya and B. Dasgupta, Fast Flavor Depolarization of Supernova Neutrinos, Phys. Rev. Lett. **126**, 061302 (2021), arXiv:2009.03337 [hep-ph].
- [68] M. Zaizen and H. Nagakura, Simple method for determining asymptotic states of fast neutrino-flavor conversion, Phys. Rev. D **107**, 103022 (2023), arXiv:2211.09343 [astro-ph.HE].
- [69] M. Zaizen and H. Nagakura, Characterizing quasisteady states of fast neutrino-flavor conversion by stability and conservation laws, Phys. Rev. D **107**, 123021 (2023), arXiv:2304.05044 [astro-ph.HE].
- [70] Z. Xiong, M.-R. Wu, S. Abbar, S. Bhattacharyya, M. George, and C.-Y. Lin, Evaluating approximate asymptotic distributions for fast neutrino flavor conversions in a periodic 1D box, Phys. Rev. D **108**, 063003 (2023), arXiv:2307.11129 [astro-ph.HE].
- [71] Y.-C. Lin and H. Duan, Collision-induced flavor instability in dense neutrino gases with energy-dependent scattering, Phys. Rev. D **107**, 083034 (2023).
- [72] S. Birol, Y. Pehlivan, A. B. Balantekin, and T. Kajino, Neutrino spectral split in the exact many-body formalism, Phys. Rev. D **98**, 083002 (2018), arXiv:1805.11767 [astro-ph.HE].
- [73] A. B. Balantekin, M. J. Cervia, A. V. Patwardhan, E. Rrapaj, and P. Siwach, Quantum information and quantum simulation of neutrino physics, European Physical Journal A **59**, 186 (2023), arXiv:2305.01150 [nucl-th].
- [74] M. Chakraborty and S. Chakraborty, Three flavor neutrino conversions in supernovae: slow & fast instabilities, J. Cosmology Astropart. Phys. **2020**, 005 (2020), arXiv:1909.10420 [hep-ph].
- [75] S. Shalgar and I. Tamborra, Three flavor revolution in fast pairwise neutrino conversion, Phys. Rev. D **104**, 023011 (2021), arXiv:2103.12743 [hep-ph].
- [76] S. Richers, D. E. Willcox, N. M. Ford, and A. Myers, Particle-in-cell simulation of the neutrino fast flavor instability, Phys. Rev. D **103**, 083013 (2021), arXiv:2101.02745 [astro-ph.HE].
- [77] H. Duan, J. D. Martin, and S. Omanakuttan, Flavor isospin waves in one-dimensional axisymmetric neutrino gases, Phys. Rev. D **104**, 123026 (2021), arXiv:2110.02286 [hep-ph].
- [78] M. Zaizen and T. Morinaga, Nonlinear evolution of fast neutrino flavor conversion in the preshock region of core-collapse supernovae, Phys. Rev. D **104**, 083035 (2021), arXiv:2104.10532 [hep-ph].

Appendix A: Normalization of the density matrix

As shown in Table II, we perform a variety of models with different dimensionality. The definition of the density matrix and Hamiltonian depends on the dimension of the momentum space. Here we explain how we calculate them.

In general, the density matrix is defined as

$$\rho_{ii} = \left(\int dX f_i \right) \left(\int dY \right) / \left(\int dX dY f_{\nu_e} \right), \quad (\text{A1})$$

where X, Y are some phase space.

1. M1 Model

In the setup of energy integrated axisymmetric case (M1), we have

$$dX = \frac{E_\nu^2 dE_\nu d\phi_\nu}{(2\pi\hbar c)^3}, \quad dY = d\cos\theta_\nu. \quad (\text{A2})$$

Then we obtain

$$\rho_{ii}(\theta_\nu) = 2 \left(\iint \frac{E_\nu^2 dE_\nu d\phi_\nu}{(2\pi\hbar c)^3} f_{\nu_i} \right) / n_{\nu_e}, \quad (\text{A3})$$

$$n_{\nu_e} = \iint \frac{E_\nu^2 dE_\nu d\Omega_\nu}{(2\pi\hbar c)^3} f_{\nu_e}. \quad (\text{A4})$$

Note that our notation assumes $\int \frac{d\cos\theta_\nu}{2} \rho = 1$ and that would be factor 2 larger than some works that assume $\int d\cos\theta_\nu \rho = 1$. The Hamiltonian is written as

$$H_{\nu\nu}(\cos\theta) = \mu \int_{-1}^1 \frac{d\cos\theta'_\nu}{2} h_{\nu\nu}, \quad (\text{A5})$$

$$h_{\nu\nu} = (\rho(\theta'_\nu) - \bar{\rho}(\theta'_\nu))(1 - \cos\theta_\nu \cos\theta'_\nu), \quad (\text{A6})$$

where $\mu = \sqrt{2}G_F n_{\nu_e}$. In Eq.(6) and collision terms, we need average neutrino energy. We define it as

$$\langle E_\nu \rangle = \left(\sum_i \iiint \frac{E_\nu^3 dE_\nu d\cos\theta_\nu d\phi_\nu}{(2\pi\hbar c)^3} f_{\nu_i} \right) / \left(\sum_i \iiint \frac{E_\nu^2 dE_\nu d\cos\theta_\nu d\phi_\nu}{(2\pi\hbar c)^3} f_{\nu_i} \right), \quad (\text{A7})$$

where $i = \nu_e, \bar{\nu}_e, \nu_\mu, \bar{\nu}_\mu$.

2. M2E Model

We call our energy dependent axisymmetric model as M2E model. The phase space is as follows.

$$dX = d\phi_\nu, dY = d\cos\theta_\nu. \quad (\text{A8})$$

The density matrix for this model is expressed as

$$\rho_{ii}(E_\nu, \theta_\nu) = 2 \left(\int f_{\nu_i}(E_\nu, \theta_\nu, \phi_\nu) d\phi_\nu \right) / n_{E, \nu_e}, \quad (\text{A9})$$

$$n_{E, \nu_e}(E_\nu) = \left(\int d\Omega_\nu f_{\nu_e} \right). \quad (\text{A10})$$

Then the Hamiltonian is

$$H_{\nu\nu}(\theta_\nu) = \int d\mu'_E \int_{-1}^1 \frac{d\cos\theta'_\nu}{2} h_{\nu\nu}. \quad (\text{A11})$$

$$d\mu_E = \sqrt{2}G_F \frac{E_\nu^2 dE_\nu}{(2\pi\hbar c)^3} n_{E, \nu_e} \quad (\text{A12})$$

$$h_{\nu\nu} = (\rho(E'_\nu, \theta'_\nu) - \bar{\rho}(E'_\nu, \theta'_\nu))(1 - \cos\theta_\nu \cos\theta'_\nu). \quad (\text{A13})$$

3. M2A Model

We call our energy integrated non-axisymmetric model as M2A model. The phase space is as follows.

$$dX = \frac{E_\nu^2 dE_\nu}{(2\pi\hbar c)^3}, \quad dY = d\cos\theta_\nu d\phi_\nu. \quad (\text{A14})$$

The density matrix for this model is expressed as

$$\rho_{ii}(\theta_\nu, \phi_\nu) = 4\pi \left(\int \frac{E_\nu^2 dE_\nu}{(2\pi\hbar c)^3} f_{\nu_i} \right) / n_{\nu_e}, \quad (\text{A15})$$

$$n_{\nu_e} = \left(\int \frac{E_\nu^2 dE_\nu d\Omega_\nu}{(2\pi\hbar c)^3} f_{\nu_e} \right). \quad (\text{A16})$$

Hamiltonian for this model is expressed as

$$H_{\nu\nu}(\theta_\nu, \phi_\nu) = \mu \int \frac{d\phi'_\nu}{2\pi} \int_{-1}^1 \frac{d\cos\theta'_\nu}{2} h_{\nu\nu}, \quad (\text{A17})$$

$$\mu = \sqrt{2}G_F n_{\nu_e} \quad (\text{A18})$$

$$h_{\nu\nu} = [\rho(\theta'_\nu, \phi'_\nu) - \bar{\rho}(\theta'_\nu, \phi'_\nu)] \times [1 - \cos\theta_\nu \cos\theta'_\nu - \sin\theta_\nu \sin\theta'_\nu \times (\cos\phi_\nu \cos\phi'_\nu + \sin\phi_\nu \sin\phi'_\nu)]. \quad (\text{A19})$$

See also Ref. [35]. As shown in Figure 7, our initial profile slightly depends on ϕ_ν but almost axisymmetric. Averaged energy is as same as Eq. (A7).

4. M3 Model

In this model, we can set $dX = 1$ and $dY = d\cos\theta_\nu d\phi_\nu$. Though we write same equations in Section II, we repeat it for completeness of this section.

We express our density matrix as

$$\rho_{ii}(E_\nu, \theta_\nu, \phi_\nu) = 4\pi f_{\nu_i}(E_\nu, \theta_\nu, \phi_\nu) / n_{E, \nu_e}, \quad (\text{A20})$$

$$n_{E, \nu_e}(E_\nu) = \int d\Omega_\nu f_{\nu_e}. \quad (\text{A21})$$

The Hamiltonian is expressed as

$$H_{\nu\nu}(\theta_\nu, \phi_\nu) = \int d\mu'_E \int \frac{d\phi'_\nu}{2\pi} \int_{-1}^1 \frac{d\cos\theta'_\nu}{2} h_{\nu\nu}, \quad (\text{A22})$$

$$d\mu'_E = \sqrt{2}G_F \frac{E_\nu'^2 dE'_\nu}{(2\pi\hbar c)^3} n_{E,\nu_e}(E_\nu), \quad (\text{A23})$$

$$h_{\nu\nu} = [\rho(E'_\nu, \theta'_\nu, \phi'_\nu) - \bar{\rho}(E'_\nu, \theta'_\nu, \phi'_\nu)] \times [1 - \cos\theta_\nu \cos\theta'_\nu - \sin\theta_\nu \sin\theta'_\nu \cos(\phi_\nu - \phi'_\nu)] \quad (\text{A24})$$

Appendix B: Code verification

In this paper, we have updated QDSCNO [42] which enables us to achieve spatial advection. For the code verification, we have tested the problem in Ref. [58] where the code comparison is performed. In the paper, 5 codes are compared, i.e., EMU [76], NuGAS [77], COSE ν [56], Bhattacharyya et al [66], and Zaizen [78].

The initial distribution is

$$\rho_{ee} = A \exp(-(\cos\theta_\nu - 1)^2/2\sigma_{ee}^2), \quad (\text{B1})$$

$$\bar{\rho}_{ee} = \bar{A} \exp(-(\cos\theta_\nu - 1)^2/2\bar{\sigma}_{ee}^2). \quad (\text{B2})$$

The σ_{ee} and $\bar{\sigma}_{ee}$ are 0.6 and 0.53, respectively. The normalization constants A and \bar{A} are determined to meet the condition, $\int d\cos\theta_\nu \rho_{ee} = 1$ and $\int d\cos\theta_\nu \bar{\rho}_{ee} = 0.9$. The notation is factor 2 different from ours, see the text below Eq. (A4). ρ_{xx} and $\bar{\rho}_{xx}$ are 0. The Hamiltonian is written as $H_{\nu\nu}(\cos\theta) = \mu \int_{-1}^1 d\cos\theta'_\nu (\rho - \bar{\rho})(1 - \cos\theta_\nu \cos\theta'_\nu)$.

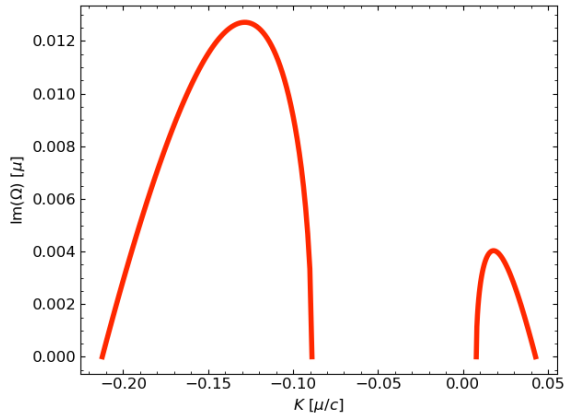


FIG. 15. The dispersion relation of the initial profile of Eqs. (B1) and (B2).

We calculate the dispersion relation using the code in NuGAS [77]. The dependence of the wavenumber on the growth rate is shown in Figure 15. There are

two branches of the solution. One appears $-0.2\mu/c < K < -0.1\mu/c$ and the other appears in $0.01\mu/c < K < 0.04\mu/c$. The former one has larger growth rate and its peak is 0.013μ . The latter one has smaller peak with 0.004μ . At $K = 0$, we do not have unstable mode and we do not expect FFC in the homogeneous model.

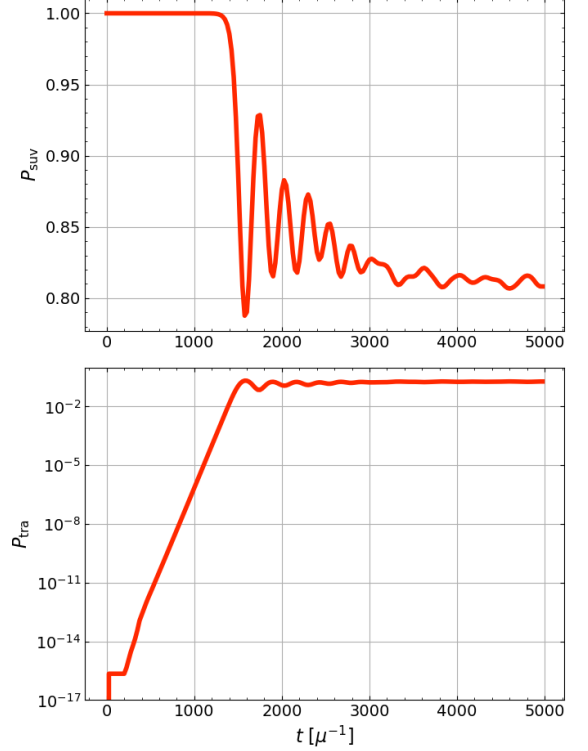


FIG. 16. The survival probability (top) and the transition probability (bottom) of the test problem in Ref. [58].

In this test, we use $N_{\theta_\nu} = 200$ bins in θ_ν with Gauss-Legendre grid. We adopt a simulation box of size $L = 10240c/\mu$ spanned by a uniform grid of $N_z = 10240$ cells. We take the unit of $c = 1$ and $\mu = 1$. The initial perturbation is the same as Eqs. (7) and (8) in Ref. [58].

In Figure 16, we show the survival probability (top) and the transition probability (bottom). The curves are very close the reference ones, Figure 1 in Ref. [58]. In the non-linear phase, the first peak comes at $t \sim 1600/\mu$ and the final survival probability is ~ 0.81 (see the top panel). The evolution in linear growth phase is also very similar to the reference one (see the bottom panel). From the dispersion relation, the most rapidly growing mode is $\text{Im}(\Omega) \sim 0.013\mu$ at $K = -0.13\mu/c$. The linear growth rate estimated from the evolution of P_{tra} is $\Omega \sim 0.026\mu$. The growth rate in P_{tra} is generally factor 2 higher than that in the dispersion relation. The simulation results are consistent with the dispersion relation. See also Figure 5 and the main text for the details.